ICAS 2021 SHANGHAI
International Council of the Aeronautical Sciences
32nd Congress of the International Council of the Aeronautical Sciences
September 6-10, 2021
Pudong Shangri-La, Shanghai, China

ANALYSIS OF AERODYNAMIC CHARACTERISTICS OF PROPELLER AT LOW ADVANCE RATIO USING A WHIRING ARM

Yuto Itoh[1] & Atsushi Satoh[2]

[1]Graduate School of Engineering, Iwate University, 4-3-5 Ueda, Morioka City, Iwate 020-8551, Japan.
[2]Faculty of Science and Engineering, Iwate University, 4-3-5 Ueda, Morioka City, Iwate 020-8551, Japan.

Abstract

A whirling arm is an effective device to measure propeller characteristics at low advance ratios. However, propeller wakes induce additional airspeed fields to the propeller circling on the whirling arm, causing fluctuation of the characteristics. This paper proposes the modeling of the induced velocity of propeller wakes and the correction of propeller characteristics obtained by the whirling arm. The effectiveness of the both results were evaluated by applying the numerical investigation and application to the experimental data.

Keywords: Whirling arm, Aerodynamic characteristics of propellers, Low advance ratio

1. Introduction

Modeling propeller characteristics takes an important part in modeling and control of multi-rotor UAVs. The characteristics at low advance ratios deeply affect their dynamics because they usually fly at low airspeed or hover.

Wind tunnel experiments are adopted for measuring the characteristics at low advance ratios[1][2][3]. However, wind tunnels have a lower speed limit of a steady airflow, and the slower the airflow, the greater turbulence. Because of this fundamental difficulty, the characteristics at low advance ratios is not well-investigated, even today.

A use of a whirling arm is a potential idea to overcome the difficulty of the wind tunnel experiment. The whirling arm can independently control the rotational speed of the propeller and the arm without any lower speed limit. The authors investigated the characteristics by using a whirling arm in the preceding works[4][5]. These results showed that the whirling arm can measure the characteristics even if the advance ratio is near zero or negative. In these works, the authors adopted an apparent advance ratio, a ratio of a rotational speed of the propeller to that of the arm, as an advance ratio of the propeller.

However, in the reality, propeller wakes induce velocity fields around blade elements, causing fluctuation of the characteristics. The advance ratio and the characteristics are needed to be corrected by considering aerodynamic effects of the propeller wakes.

The purpose of this paper is twofold. The first one is to provide aerodynamic characteristics model of the propeller circling on the whirling arm, considering velocity fields induced by surrounding vortices. The second one is to propose the correction of the characteristics obtained by the whirling arm. In the modeling, the velocity field of the propeller wakes is modeled as that of moving helical vortex tubes.

The induced velocities model is applied to the calculation of the characteristics. In this work, the characteristics of three types of propellers at the advance ratio from 0.00 to about 0.60 are considered. The characteristics are determined by hybrid blade element momentum theory (HBEMT).

Furthermore, we measure the characteristics at the advance ratio from 0.00 to about 0.40 for three types of propellers. We propose a correction for the characteristics and adopted the proposed method to data obtained by the whirling arm experiments.

2. Modeling

We firstly discuss the modeling of velocity fields of propeller circling on a whirling arm. Next, the propeller characteristics are determined based the proposed airspeed model. Detail of the modeling can be found in the authors' work[6].

2.1 Problem Setting

Figure 1 shows the structure of the whirling arm to measure the propeller characteristics. A rotary shaft is a vertical shaft which rotates with a constant angular velocity ω_w. The whirling arm is a cantilever that is horizontally attached to the rotary shaft. The propeller (diameter D_p and number of blades B) is attached on a far end of the arm. This propeller rotates with a constant angular velocity ω_p, and generates thrust T and torque Q. A rotation axis of the propeller is aligned to a tangent line of a circling orbit of the center of the propeller. A distance from the center of the propeller to the z_w axis (i.e. a radius of the propeller circling orbit) is l_w.

We use three coordinate systems to model velocity fields in this paper. Firstly, blade coordinate systems $O_p - ({}^ir_p, {}^i\psi_p, {}^iz_p)$ shown in Figure 1 are defined to represent positions of the blade elements of the i th blade, where $i = 1, 2, \cdots, B$ is the index of the blade. An ${}^ir_p$ axis is set along the i th blade and rotates with the blade. A ${}^iz_p$ axis is set to coincide with the rotation axis of the propeller. An angle ${}^i\psi_p$ denotes a rotation of the i th blade from a vertical upward position. We refer to O_p as a "propeller position".

Secondly, an arm coordinate system $O_w - (r_w, \psi_w, z_w)$ is defined as shown in Figure 1. The z_w axis is set to coincide with the rotation axis of the rotary shaft, therefore it is perpendicular to the rotation surface of the arm. The origin O_w is the center of the circling orbit of O_p. An angle ψ_w is a rotation angle of the arm. The r_w axis is defined from O_w toward O_p.

Thirdly, a vortex filament coordinate system is defined. Let us assume that the propeller wake consists of b helical vortex filaments. The vortex filament coordinate system ${}^iO_m^{(j,k)} - ({}^ir_h^{(j,k)}, {}^i\psi_h^{(j,k)}, {}^iz_h^{(j,k)})$ is defined for the k $(k = 1, 2, \cdots, b)$ th filament in the j $(j = 1, 2, \cdots)$ th wake, as shown in Figure 2.

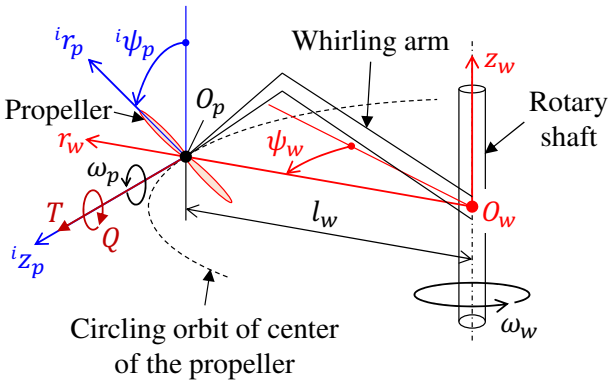

Figure 1 – Whirling arm model

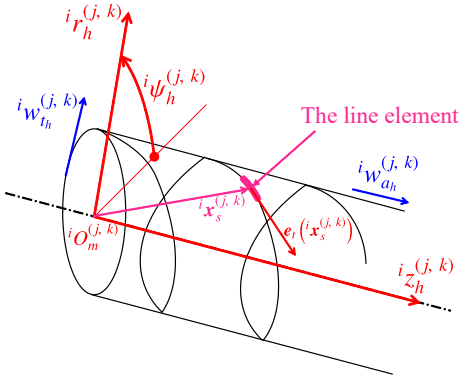

Figure 2 – Vortex filament coordinate system

We refer to ${}^iO_m^{(j,k)}$ as a "position of the k th filament in the j th wake to the i th blade". A position vector from ${}^iO_m^{(j,k)}$ to a line element on the vortex filament is denoted as ${}^i\boldsymbol{x}_s^{(j,k)}({}^ir_h^{(j,k)}, {}^i\psi_h^{(j,k)}, {}^iz_h^{(j,k)})$. A vector $\boldsymbol{e}_t({}^i\boldsymbol{x}_s^{(j,k)})$ denotes a unit tangent vector of the helical vortex filament. A position vector from ${}^iO_m^{(j,k)}$ to the blade element at the radius r_p of the i th blade is represented as ${}^i\boldsymbol{x}_h^{(j,k)}({}^ir_p)$.

All vortex filaments in the j th wake move along the ${}^iz_h^{(j,k)}$ axis with individual velocities. Each filament has a constant axial velocity ${}^iw_{a_h}^{(j,k)}$ and a constant tangential velocity ${}^iw_{t_h}^{(j,k)}$. Denote the time when the j th wake is generated as t_j. These velocities are set to be identical to induced velocities at the k th blade element when the j th wake is generated, namely, ${}^iw_{a_h}^{(j,k)} = v_a({}^ir_p)\big|_{t=t_j}$, ${}^iw_{t_h}^{(j,k)} = v_t({}^ir_p)\big|_{t=t_j}$. The ${}^iO_m^{(j,k)}$ also moves along the ${}^iz_h^{(j,k)}$ axis with a same axial velocity of the corresponding vortex filament. A reference of ${}^i\psi_h^{(j,k)}$ is the position of the i th blade when $t = t_j$.

Figure 3 shows a positional relationship between the propeller and the j th wake. Note that only the k th helical vortex filament is shown in Figure 3. A differential angle between the position of the

propeller and the position of the k th filament in the j th wake to i th blade is defined as

$$\Delta^i\psi_w^{(j,k)} = \angle O_p O_w {}^iO_m^{(j,k)} = \psi_w - \psi_{w_h}^{(j)} + \arctan\left[\frac{{}^id_h^{(j,k)}}{l_w}\right], \tag{1}$$

where ${}^id_h^{(j,k)} = {}^iw_{a_h}^{(j,k)} \cdot (s-j) \cdot \Delta t$ denotes a distance traveled by the k th vortex filament in $(t - t_j)$. An angle $\psi_{w_h}^{(j)}$ denotes the rotation angle of the arm when the j th wake was generated.

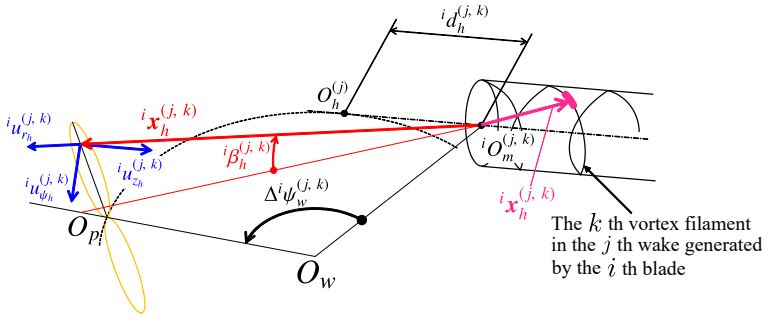

Figure 3 – Propeller wake with induced velocity profiles

The k th vortex filament included in the j th wake to the i th blade induces a velocity field ${}^iu_h^{(j,k)} = [{}^iu_{r_h}^{(j,k)}, {}^iu_{\psi_h}^{(j,k)}, {}^iu_{z_h}^{(j,k)}]$. The velocity field of the j th wake is the sum of the induced velocity fields of all vortex filaments included in the j th wake.

2.2 Airspeed Modeling

The aforementioned vortices induce airspeed to fluctuate the actual advance ratio. We model the airspeed using a vortex method to derive the local aerodynamic characteristic of the blade element. We denote the airspeed of the blade element of the i th blade as $\boldsymbol{U}({}^ir_p) = [U_a({}^ir_p), U_t({}^ir_p)]$. According to a discussion so far,

$$U_a\left({}^ir_p\right) = \left(l_w + {}^ir_p \cdot \sin{}^i\psi_p\right) \cdot \omega_w + u_{a_h}\left({}^ir_p\right), U_t\left({}^ir_p\right) = {}^ir_p \cdot \omega_p + u_{t_h}\left({}^ir_p\right). \tag{2}$$

The first terms of the right-hand side of (2) represent the induced airspeed components from a mechanical rotation of the propeller and the arm. The second terms represent airspeed components induced by propeller wakes.

2.3 Modeling of Airspeed Induced by Propeller Wakes

Under an assumption that the propeller wake never diffuses nor connect with other wakes, the propeller wake has been modeled as a cylindrical semi-infinite helical vortex tube. Okulov *et al.*[7] proposed an induced velocity model of a helical vortex tube. Based on their ideas, we model the velocity field which multiple helical vortex tubes induce to blade elements on the circling propeller.

We represent ${}^i\boldsymbol{u}_h^{(j,k)}({}^ir_p)$ as an induced velocity around the blade element at the radius r_p of the i th blade. This is obtained by integrating the differential induced velocities of the line element, $d^i\boldsymbol{u}_h^{(j,k)} = \left[d^iu_{r_h}^{(j,k)}, d^iu_{\psi_h}^{(j,k)}, d^iu_{z_h}^{(j,k)}\right]$, over the helical vortex filament. According to the Biot-Savart law[8], $d^i\boldsymbol{u}_h^{(j,k)}$ is given by,

$$d^i\boldsymbol{u}_h^{(j,k)}\left({}^i\boldsymbol{x}_h^{(j,k)}\right) = \nabla \times \left(\frac{{}^i\Gamma_h^{(j,k)}\left({}^i\boldsymbol{x}_h^{(j,k)}\right)}{4\pi} \cdot \frac{\boldsymbol{e}_t\left({}^i\boldsymbol{x}_s^{(j,k)}\right)}{\left\|{}^i\boldsymbol{x}_h^{(j,k)} - {}^i\boldsymbol{x}_s^{(j,k)}\right\|} dl\right), \tag{3}$$

where ${}^i\Gamma_h^{(j,k)}$ and ∇ denote a circulation around a central axis of the line filament and a differential operator in the cylindrical coordinate system. The velocity field induced by a filament is given by,

$$ {}^i\boldsymbol{u}_h^{(j,k)}\left({}^ir_p\right) = \int_s \left[\frac{d^i\boldsymbol{u}_h^{(j,k)}\left({}^i\boldsymbol{x}_h^{(j,k)}\left({}^ir_p\right)\right)}{ds}\right] ds. \tag{4}$$

We adopt a Kapteyn series model of (4) in numerical investigation. See Okulov *et al.* [7] for a detailed derivation.
By using the components of ${}^{i}\boldsymbol{u}_h^{(j,k)}$, axial and tangential components of the induced velocity at the i th blade element are expressed as follows,

$$
\begin{aligned}
{}^{i}V_{a_h}^{(j,k)}({}^{i}r_p) &= {}^{i}u_{z_h}^{(j,k)}({}^{i}r_p)\cos\Delta^{i}\psi_w^{(j,k)} + \left[{}^{i}u_{r_h}^{(j,k)}({}^{i}r_p)\cos{}^{i}\beta_h^{(j,k)}({}^{i}r_p) + {}^{i}u_{\psi_h}^{(j,k)}({}^{i}r_p)\sin{}^{i}\beta_h^{(j,k)}({}^{i}r_p)\right]\sin\Delta^{i}\psi_w^{(j,k)}, \quad (5)\\
{}^{i}V_{t_h}^{(j,k)}({}^{i}r_p) &= \left[{}^{i}u_{\psi_h}^{(j,k)}({}^{i}r_p)\cos{}^{i}\beta_h^{(j,k)}({}^{i}r_p) - {}^{i}u_{r_h}^{(j,k)}({}^{i}r_p)\sin{}^{i}\beta_h^{(j,k)}({}^{i}r_p)\right]\cos{}^{i}\psi_p + \left[{}^{i}u_{z_h}^{(j,k)}({}^{i}r_p)\sin\Delta^{i}\psi_w^{(j,k)}\right.\\
&\quad \left.-\left\{{}^{i}u_{r_h}^{(j,k)}({}^{i}r_p)\cos{}^{i}\beta_h^{(j,k)}({}^{i}r_p) + {}^{i}u_{\psi_h}^{(j,k)}({}^{i}r_p)\sin{}^{i}\beta_h^{(j,k)}({}^{i}r_p)\right\}\cos\Delta^{i}\psi_w^{(j,k)}\right]\sin{}^{i}\psi_p, \quad (6)
\end{aligned}
$$

where

$$
{}^{i}\beta_h^{(j,k)}\left({}^{i}r_p\right) = \arcsin\left[\frac{{}^{i}r_p\cdot\cos{}^{i}\psi_p}{\left\|{}^{i}\boldsymbol{x}_h^{(j,k)}\left({}^{i}r_p\right)\right\|}\right]. \quad (7)
$$

Based on (5) and (6), we obtain the airspeed induced by the propeller wakes at $t = t_s$ represented as follows,

$$
u_{a_h}\left({}^{i}r_p\right) = \sum_{l=1}^{B}\sum_{m=1}^{s+1}\sum_{n=1}^{b}\left[{}^{l}V_{a_h}^{(m,n)}\left({}^{i}r_p\right)\right],\ u_{t_h}\left({}^{i}r_p\right) = \sum_{l=1}^{B}\sum_{m=1}^{s+1}\sum_{n=1}^{b}\left[{}^{l}V_{t_h}^{(m,n)}\left({}^{i}r_p\right)\right]. \quad (8)
$$

2.4 Propeller Charcteristics

Thrust coefficient C_T, torque coefficient C_Q, and propulsion efficiency η are defined as follows,

$$
C_T = \frac{T}{\rho\cdot\left(n_p\right)^2\cdot\left(D_p\right)^4},\ C_Q = \frac{Q}{\rho\cdot\left(n_p\right)^2\cdot\left(D_p\right)^5},\ \eta = \frac{1}{2\pi}\cdot J\cdot\frac{C_T}{C_Q}, \quad (9)
$$

where J denotes the advance ratio, and is defined as follows,

$$
J = \frac{1}{B}\sum_{i=1}^{B}\left[\frac{U_a({}^{i}\tilde{r}_p)}{U_t({}^{i}\tilde{r}_p)}\right], \quad (10)
$$

where $\tilde{r}_p$ denotes a representative radius. In the whirling arm, the fluctuation of ${}^{i}J$ results from a periodic change of an axial airspeed component caused by the periodic change of the radial position of the blades. Note that J gives the instantaneous advance ratio and it is not constant even in steady state.
From a viewpoint of the measurement of the propeller characteristics, we want to obtain a representative value of the advance ratio (i.e. constant J). We propose to adopt an average of J for a period of the propeller rotation as a representative advanced ratio in whirling arm experiments,

$$
J_r = \frac{1}{f_p}\int_{t-f_p}^{t} J(\tau)\,d\tau, \quad (11)
$$

where $f_p = 2\pi/\omega_p$. Definitions in (9) are usually applied to wind tunnel experiments. On the other hand, we applied the hybrid blade element momentum theory to determine an appropriate C_T and C_Q in our problem setting (see §2.5).

2.5 Propeller Modeling

We use the hybrid blade element momentum theory (HBEMT) for the propeller modeling. The HBEMT is a modeling method based on blade element momentum theory (BEMT) and blade element theory (BET). The HBEMT is useful to analyze the propeller aerodynamics in non-hover flights. Khan *et al.*[9] applied the HBEMT to an analysis of the propeller aerodynamics in a forward flight. This paper uses the HBEMT to determine axial and tangential induced velocities which vary with respect to r_p for every time step.

Let us define the nonlinear optimization problem using a non-dimensional radius of the i th blade, ${}^i\hat{r}_p = (2\cdot {}^i r_p)/D_p$. Denote the root position as ${}^i\hat{r}_{p,root}$, and the tip position as ${}^i\hat{r}_{p,tip}$. Then, ${}^i\hat{v}_a[k] = {}^i\hat{v}_a({}^i\hat{r}_p[k])$, ${}^i\hat{v}_t[k] = {}^i\hat{v}_t({}^i\hat{r}_p[k])$ $(k = 1,\ 2,\ \cdots,\ b)$ are determined by solving the following nonlinear optimization problem for each blade $i = 1, \cdots, B$.

Problem 1. *For given* ${}^i\hat{r}_p[k]$, ${}^i\hat{r}_p[1] < \cdots < {}^i\hat{r}_p[b]$, ${}^i\hat{r}_p[1] = {}^i\hat{r}_{p,root}$, ${}^i\hat{r}_p[b] = {}^i\hat{r}_{p,tip}$, *find* ${}^i\hat{v}_a[k]$, ${}^i\hat{v}_t[k]$, *s.t.* (12)

$$\left[\frac{d^iC_T({}^i\hat{r}_p[k])}{d^i\hat{r}_p}\right]_{BEMT}\left({}^i\hat{v}_a[k], {}^i\hat{v}_t[k]\right) = \left[\frac{d^iC_T({}^i\hat{r}_p[k])}{d^i\hat{r}_p}\right]_{BET}\left({}^i\hat{v}_a[k], {}^i\hat{v}_t[k]\right),$$
$$\left[\frac{d^iC_Q({}^i\hat{r}_p[k])}{d^i\hat{r}_p}\right]_{BEMT}\left({}^i\hat{v}_a[k], {}^i\hat{v}_t[k]\right) = \left[\frac{d^iC_Q({}^i\hat{r}_p[k])}{d^i\hat{r}_p}\right]_{BET}\left({}^i\hat{v}_a[k], {}^i\hat{v}_t[k]\right).$$

Left sides of (12) are non-dimensional aerodynamic distributions derived from the BEMT (see Adkins *et al.*[10]). Right sides of (12) are the non-dimensional aerodynamic distributions derived from the BET (see McCormick *et al.*[11]).
Once suitable ${}^i\hat{v}_a({}^i\hat{r}_p)$ and ${}^i\hat{v}_t({}^i\hat{r}_p)$ are found from Problem 1, we can determine representative values of the thrust and torque coefficients of the i th blade as follows,

$$C_{T_r}(t) = \sum_{i=1}^{B}\left(\frac{1}{f_p}\int_{t-f_p}^{t}\int_{\hat{r}_{p,root}}^{\hat{r}_{p,tip}}\left[\frac{d^iC_T({}^i\hat{r}_p)}{d^i\hat{r}_p}\right]_{BET} d^i\hat{r}_p d\tau\right),\ C_{Q_r}(t) = \sum_{i=1}^{B}\left(\frac{1}{f_p}\int_{t-f_p}^{t}\int_{\hat{r}_{p,root}}^{\hat{r}_{p,tip}}\left[\frac{d^iC_Q({}^i\hat{r}_p)}{d^i\hat{r}_p}\right]_{BET} d^i\hat{r}_p d\tau\right). \quad (13)$$

where $f_p = (2\pi)/\omega_p$ denotes a period of a propeller rotation.

3. Numerical Investigation

We performed a numerical investigation to evaluate the validity of the model. In this section, methods and settings for the calculation are discribed.

3.1 Discretization

The numerical calculation requires a discretization of the rotation of the blades and the arm. Figure 4 shows discretized process of temporal evolution of the wake.
The wake of the circling propeller shapes an outward spiral from the circling orbit. In this work, the spiral wake is modeled by finite length straight wakes which are tangentially moving apart from the circling orbit with constant velocities. Figure 4 shows the evolution process of this “discrete wake model”.
Note that if ω_w is sufficiently smaller than the axial velocity of the wake, as is often the case with the measurement of the propeller characteristics at low advance ratios, the propeller does not plunge into the wake separated during the previous round.
For a given time step Δt, the time is discretized as $t_s = \Delta t \cdot s$, where $s = 0,\ 1,\ \cdots$ is called “step". As the propeller advances by the rotation of the arm, wakes are generated and separated from the blades on every Δt.
The first wake is generated at $t = 0$. At $t = t_s$, $(s+1)$ wakes exist, and rotation angle of the arm is $\psi_w = \omega_w \cdot s \cdot \Delta t$. As shown in Fig. 4, generated wakes are indexed as $j = 1, 2, \cdots, s$. Helical vortex filaments are also indexed as $k = 1, 2, \cdots, b$, numbered from the center outward, as shown in Fig. 5.
An initial rotation angle of the i th blade is denoted as ${}^i\psi_{p_0}$. A rotation angle of the i th blade at the s th step is defined as,

$${}^i\psi_p[s] = {}^i\psi_{p_0} + \omega_p \cdot \Delta t \cdot s\ ,\ {}^i\psi_{p_0} = {}^i\psi_p[0] = \frac{2\pi\cdot(i-1)}{B}. \quad (14)$$

The discretized rotation angle of the arm $\psi_w[s]$ is similarly expressed as (14) for $(\psi_{w_0},\ \omega_w)$.

3.2 Calculation flow

Figure 6 shows the calculation flow in the numerical investigation. Initial values of variables are as follows,

$$\text{For } s \le 0,\ \ \tilde{J}[s] = 0,\ \bar{J}[s] = 0,\ \boldsymbol{u}_h = \boldsymbol{0},\ \boldsymbol{u}_w = \boldsymbol{0}. \quad (15)$$

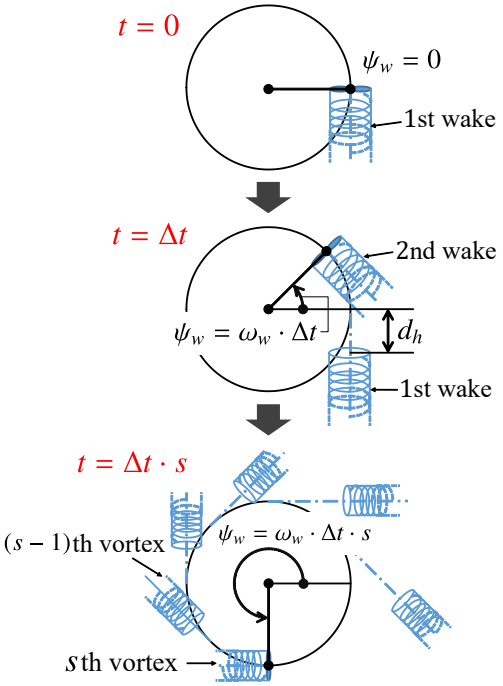

Figure 4 – Wake evolution process

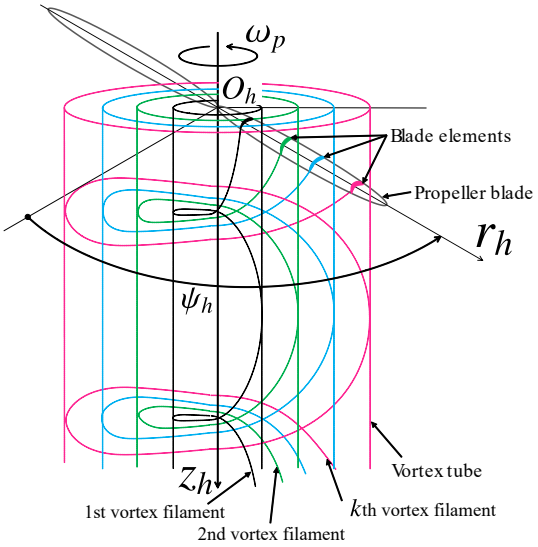

Figure 5 – Coordinate system and parameters of the helical vortex filaments

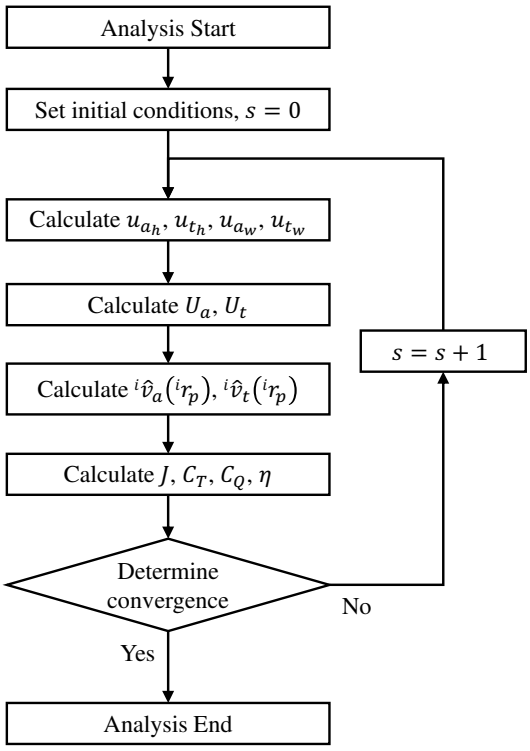

Figure 6 – Calculation flow

The calculation should be executed until a convergence of the advance ratio is confirmed. In the "Determine convergence" block shown in Fig 6, we introduce an average of $\tilde{J}_r$ for a period of an arm rotation to check whether the iteration has reached a steady state. For a small $\delta > 0$, let us define the convergence condition as

$$\bar{J}_r[s] = \frac{1}{s_w} \sum_{p=s-s_w}^{s} \left(\frac{1}{s_p} \sum_{p=s-s_p}^{s} J[p] \right), \quad \left\| \frac{\bar{J}_r[s] - \bar{J}_r[s-1]}{\bar{J}_r[s]} \right\| < \delta, \tag{16}$$

where $s_p = \lceil (2\pi)/(\omega_p \cdot \Delta t) \rceil$, $s_w = \lceil (2\pi)/(\omega_w \cdot \Delta t) \rceil$. If the termination condition in Eq. (16) is not satisfied, update s and repeat the calculation.
We adopt $\bar{J}_r$ in (16) as the representative value of the advance ratio in the numerical investigation. We also define representative values of C_T and C_Q as follows,

$$\bar{C}_{T_r}[s] = \frac{1}{s_w} \sum_{p=s-s_w}^{s} \left(\frac{1}{s_p} \sum_{p=s-s_p}^{s} C_T[p] \right), \; \bar{C}_{Q_r}[s] = \frac{1}{s_w} \sum_{p=s-s_w}^{s} \left(\frac{1}{s_p} \sum_{p=s-s_p}^{s} C_Q[p] \right). \tag{17}$$

A representative value of a discretized propulsion efficiency $\bar{\eta}_r$ is calculated by applying $\bar{J}_r$, $\bar{C}_{T_r}$, and $\bar{C}_{Q_r}$ to η in (9).

4. Experimental Investigation

We describe a used whirling arm apparatus and a method for measuring the propeller characteristics in this section.

4.1 Whirling Arm Apparatus

Figure 7 shows the whirling arm apparatus used in the experimental investigation. Table 1 shows the primary specification of this apparatus. This apparatus has a force/moment sensor at an end of the whirling arm to measure the thrust and the torque of target propellers. A supporting rod for the propulsion system is attached on the force/moment sensor. Note that the arm is not perpendicular to the supporting rod so that the direction of the relative wind at the propellers is orthogonal to the rotation plane of the propeller.

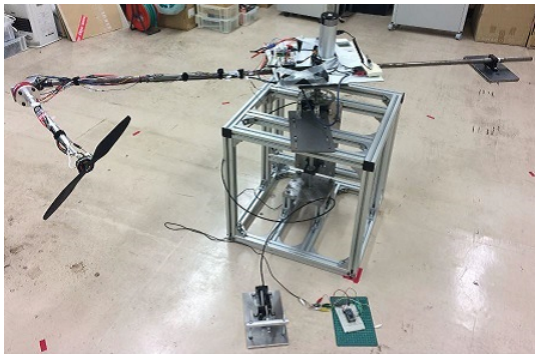

Figure 7 – Whirling arm apparatus

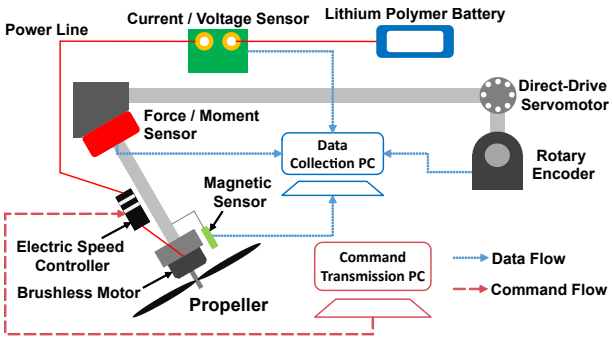

Figure 8 – Measurement system

Table 1 – The primary specification

Item	Value
Length of the arm	1.635 m
Tuning radius of a propeller	1.464 m
Height of a propeller from the ground	1.000 m
Input voltage power of direct-drive motor	200 V
Rated output power of direct-drive motor	550 W

Figure 8 shows the control and measurement system of the whirling arm apparatus. A direct-drive servomotor attached to a rotary shaft of the arm rotates the arm at a desired rotational speed.

A current/voltage sensor connected to an electric speed controller measures a power consumption of the brushless motor driving target propellers. A rotary encoder attached to a rotary shaft of the arm measures an angular velocity of the rotating arm. A magnetic sensor attached to a side of a brushless motor measures a rotation number of target propellers.
A PC on the apparatus ("Data collection PC" in Figure 8) receives and saves data of each sensor. A ground PC ("Command transmission PC" in Figure 8) remotely control the data collection PC using a remote desktop application. We can set the desired rotational speed of the arm and the propeller from the command transmission PC.

4.2 Correction of the apparent advance ratio

During a steady operation (i.e. ω_w and ω_p are constant respectively), a positional relationship between the propeller and the wake vortex at time t is shown in Fig. 9. The k th vortex filament in the generated wake travels at an axial velocity ${}^{i}w_a^{(j,k)}$ in the positive direction of ${}^{i}z_h^{(j,k)}$, while rotating at a tangential velocity ${}^{i}w_t^{(i,j)}$. Wake vortices extend at a velocity of ${}^{i}r_h^{(j,k)} \cdot \arctan\left[{}^{i}w_a^{(j,k)} / {}^{i}w_t^{(j,k)}\right]$ in the positive direction of the ${}^{i}z_h^{(j,k)}$ axis as they moves.
Let ${}^{i}t_h^{(j)} \leq t$ be the time when the j th wake vortex generated from the i th blade was generated. The rotation of the arm from the position where the wake was generated is expressed as

$$\Delta^{i}\psi_w^{(j)} = \omega_w \cdot \left(t - {}^{i}t_h^{(j)}\right). \tag{18}$$

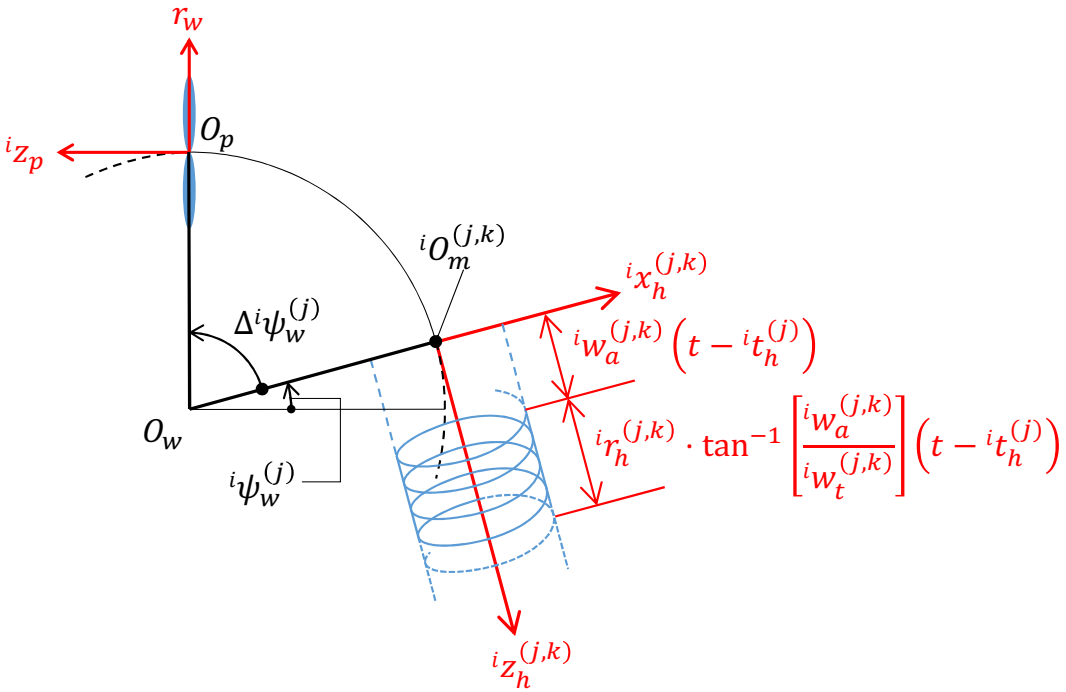

Figure 9 – The positional relationship between blades and wake vortices at t

According to Biot-Savert law, the velocity field which a line element induces to a blade element are represented as follows,

$$\boldsymbol{u}_w\left({}^{i}r_p, {}^{i}r_h, t, {}^{i}t_h^{(j)}\right) = [u_{x_w}, u_{y_w}, u_{z_w}] = \int_{{}^{i}r_h^{(j,k)}} \int_t \nabla \times \left(\frac{d^{i}\boldsymbol{A}_h^{(j,k)}}{dt}\right) dt d^{i}r_h^{(j,k)}, \tag{19}$$

where

$$\frac{d^{i}\boldsymbol{A}_h^{(j,k)}}{dt}\left({}^{i}\boldsymbol{x}_h^{(j,k)}, {}^{i}\boldsymbol{x}_s^{(j,k)}\right) = \frac{{}^{i}\Gamma_h^{(j,k)}\left({}^{i}\boldsymbol{x}_h^{(j,k)}\right)}{4\pi \cdot {}^{i}w_t^{(j,k)}} \cdot \frac{\boldsymbol{e}_t\left({}^{i}\boldsymbol{x}_s^{(j,k)}\right)}{\left\|{}^{i}\boldsymbol{x}_h^{(j,k)} - {}^{i}\boldsymbol{x}_s^{(j,k)}\right\|}. \tag{20}$$

In a steady working condition of the propeller, a vortex filament induces the axial velocity $\bar{u}_{a_w}$ and the tangential velocity $\bar{u}_{t_w}$ to the blade element. These are calculated by using following equations,

$$\bar{u}_{a_w}\left({}^{i}r_p, {}^{i}\psi_p\right) = \int_0^{\infty}\int_0^{t}\int_0^{R_h}\left[u_{a_w}({}^{i}r_p, {}^{i}r_h, t, {}^{i}t_h^{(j)})\right] dr_h dt_h dt, \tag{21}$$

$$\bar{u}_{t_w}\left({}^{i}r_p, {}^{i}\psi_p\right) = \int_0^{\infty}\int_0^{t}\int_0^{R_h}\left[u_{t_w}({}^{i}r_p, {}^{i}r_h, t, {}^{i}t_h^{(j)})\right] dr_h dt_h dt, \tag{22}$$

where

$$u_{a_h} = u_z \cdot \cos\left(\Delta^i\psi_w^{(j)}\right) + u_x \cdot \sin\left(\Delta^i\psi_w^{(j)}\right) \tag{23}$$

$$u_{t_h} = -u_x \cdot \cos\left(\Delta^i\psi_w^{(j)}\right) \cdot \cos\left(\omega_p \cdot t\right) + u_y \cdot \sin\left(\omega_p \cdot t\right) + u_z \cdot \sin\left(\Delta^i\psi_w^{(j)}\right) \cdot \cos\left(\omega_p \cdot t\right) \tag{24}$$

Incorporating (21) and (22) with the apparent advance ratio and averaging the advance ratio of each blade with respect to the rotation angle derive a following corrected advance ratio,

$$J_{corr}(r_p) = \frac{1}{B}\sum_{i=1}^{B}\left[\frac{1}{2\pi}\int_0^{2\pi}\frac{\left(l_w + r_p \cdot \sin{}^{i}\psi_p\right)\cdot\omega_w + \bar{u}_{a_w}(r_p, {}^{i}\psi_p)}{n_p \cdot D_p + \bar{u}_{t_w}(r_p, {}^{i}\psi_p)} d^{i}\psi_p\right]. \tag{25}$$

4.3 Collecting data in steady state

Collecting data in steady state is required to obtain propeller characteristics. To get those data, the authors produce convergence criteria shown in Table 2, where $\omega_{w_{ref}}$ denotes an angular rate of the arm set by experimenters, and $n_{p_{ref}}$ a rotation number of the propeller set by them.
The authors extracted the data contained in time intervals that satisfy all criteria shown in Table 2 are satisfied. An example of the aerodynamic data in steady state and data collect phases is presented in Fig. 10.

Table 2 – Convergence criteria

Criteria	Minimum duration
$\|1-(\omega_{w_{ref}}/\omega_w)\| \leq 0.02$	15.0 s
$\|1-(n_{p_{ref}}/n_p)\| \leq 0.05$	15.0 s

5. Results and Discussion

Target propellers and conditions are firstly described in this chapter. Next, obtained propeller characteristics are presented.

5.1 Target propellers

For the analysis, propellers designed for small UAVs are selected. Table 3 shows the specifications. All propellers have two blades (i.e. $B = 2$). Figure 11 shows radial distribution of the non-dimensional chord $\hat{c}_p = (c_p/R_p)$ of them, and Fig. 12 that of the pitch angle θ_p. These figures are reproduction from open-access data of propeller geometry on the UIUC Propeller Data Site.[12]

Table 3 – Target propeller specification

Propeller	Diameter	Pitch	Airfoil[3]
APC10x5E	0.2540 m	0.1270 m	NACA4412
APC11x4.5E	0.2794 m	0.1397 m	NACA4412
APC10x4.7SF	0.2540 m	0.1194 m	Clark Y

5.2 Conditions in numerical investigation

Table 4 shows the working conditions of the propeller and the whirling arm in the numerical investigation.
In order to accurately grasp the convergence of the velocity field, Δt should be set to be sufficiently smaller than the period of a rotation of the propeller. Here we set the values of Δt to less than $1/3$ of f_p. We also set δ in Eq. (16) to $\delta = 3.5 \times 10^{-5}$ for all cases.

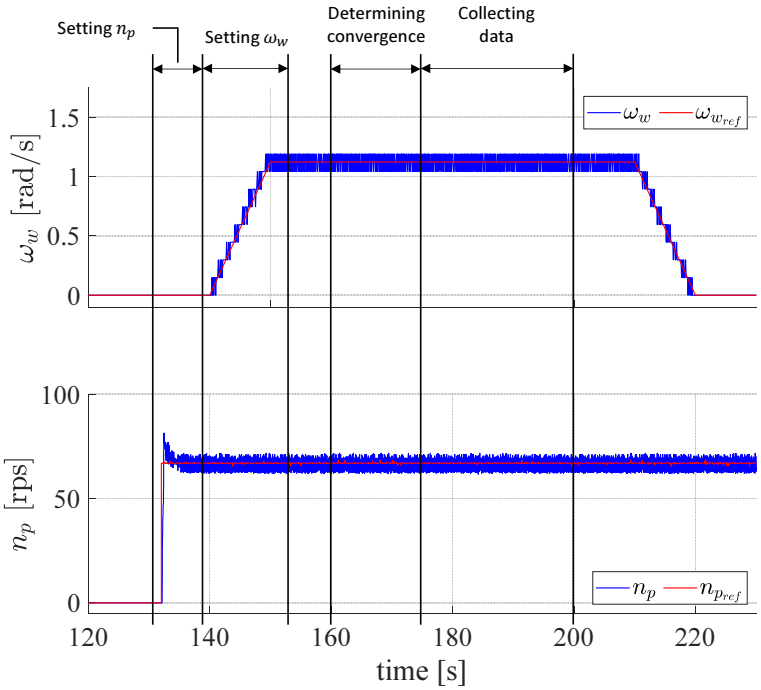

Figure 10 – Time history of ω_w and n_p

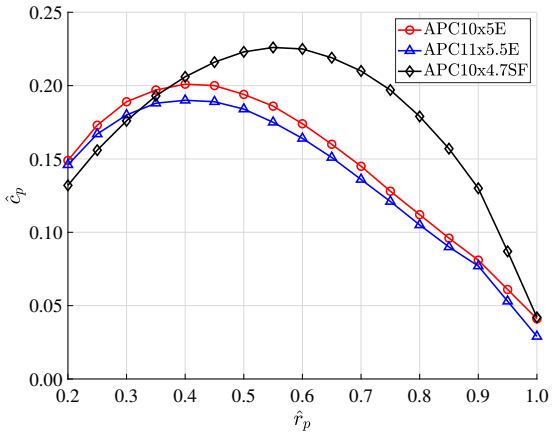

Figure 11 – Radial distribution of the non-dimensional chord

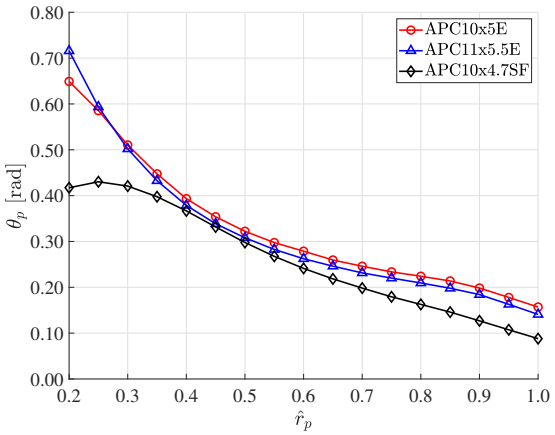

Figure 12 – Radial distribution of the blade pitch angle

Table 4 – Working conditions

Items	Description	Values
ρ	density of air	$1.225\ \mathrm{kg/m^3}$
l_w	arm's length	$1.464\ \mathrm{m}$

5.3 Experiment Environment

The electric propulsion system to be measured consists of components shown in Table 5. Target propellers are equivalent to them shown in Table 3.

Table 5 – Components of the electric propulsion system

Components	Name of parts
Brushless DC motor	Hacker A30-24M-UAV
Electric speed controller	Hacker JETI model HI Copter 40A Opto

5.4 Operating conditions

Table 6 shows conditions for rotation numbers of each propeller in both investigation. These were selected to compare measured characteristics with results in UIUC database[12].

Table 6 – Conditions for rotation numbers of each propeller

Propeller	rotation numbers
APC10x5E	4000 rpm, 5000 rpm, 6000 rpm
APC11x4.5E	3000 rpm, 4000 rpm, 5000 rpm
APC10x4.7SF	4000 rpm, 5000 rpm, 6000 rpm

For each rotation numbers of propellers, angular rates of the arm are set to achieve apparent advance ratio shown below,

$$J_{app} = 0.00,\ 0.05,\ 0.10,\ 0.15,\ 0.20,\ 0.25,\ 0.30,\ 0.35,\ 0.40$$

5.5 Calculated Propeller Characteristics

Figure 13–21 show the propeller characteristics obtained from the numerical investigation. Horizontal error bars show the standard deviation of advance ratio during the last rotation of the arm. Vertical error bars show the standard deviation of the characteristics during the last rotation of the arm. For comparison, these plots also show the results from the wind tunnel experiments by UIUC (Brandt et al.[12]).

We can see the characteristics obtained through the proposed model keep better consistency with the results of UIUC. This tendency suggests that the proposed model has a potential to appropriately correct the advance ratio for the whirling arm experiments.

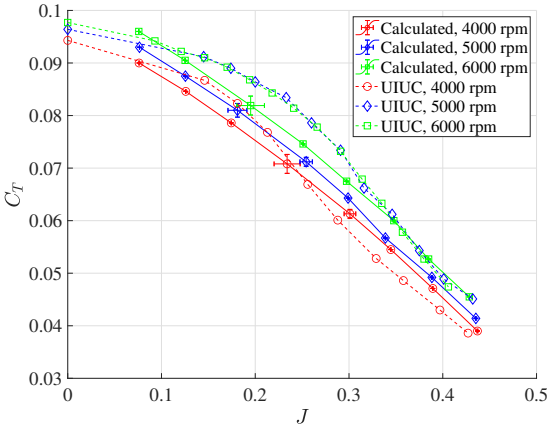

Figure 13 – Calculated thrust coefficient curve of APC10x5E

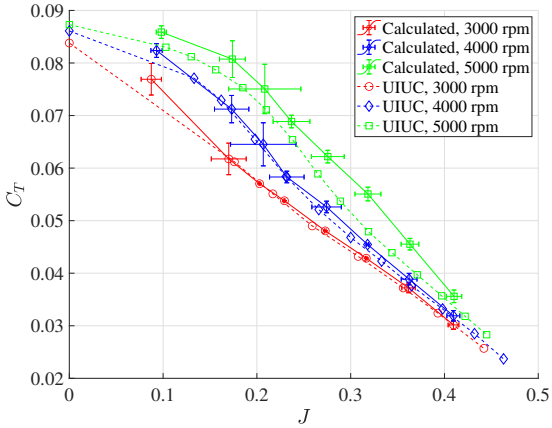

Figure 14 – Calculated thrust coefficient curve of APC11x4.5E

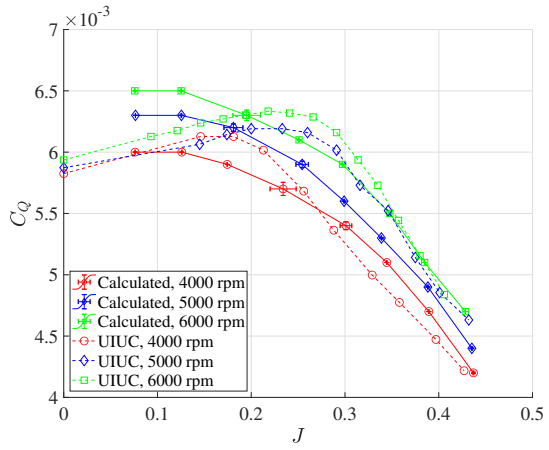

Figure 15 – Calculated torque coefficient curve of APC10x5E

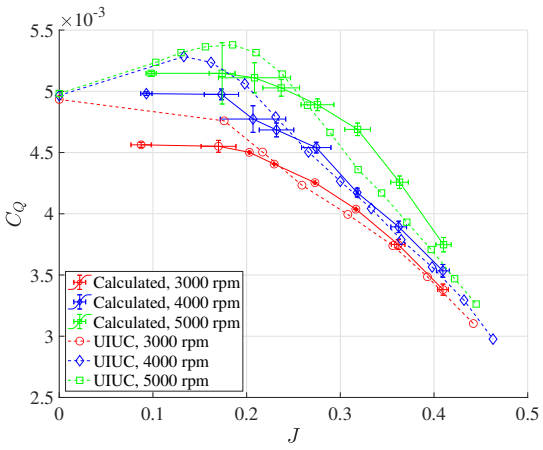

Figure 16 – Calculated torque coefficient curve of APC11x4.5E

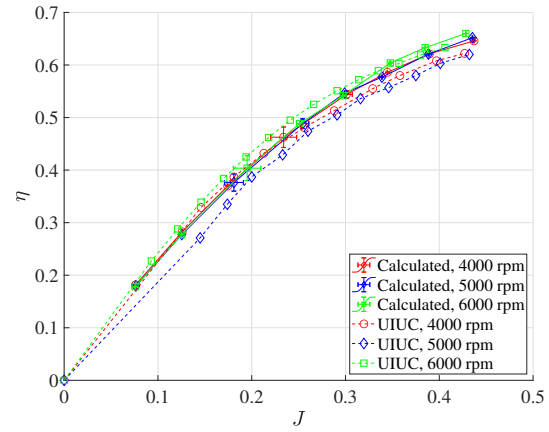

Figure 17 – Calculated propulsion efficiency curve of APC10x5E

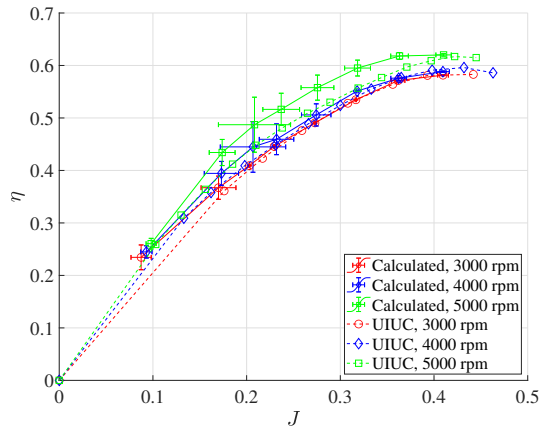

Figure 18 – Calculated propulsion efficiency curve of APC11x4.5E

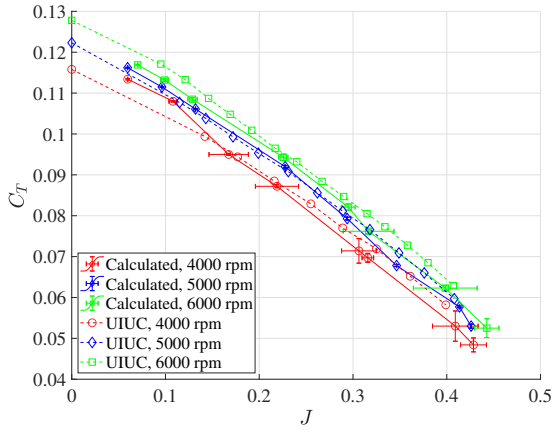

Figure 19 – Calculated thrust coefficient curve of APC10x4.7SF

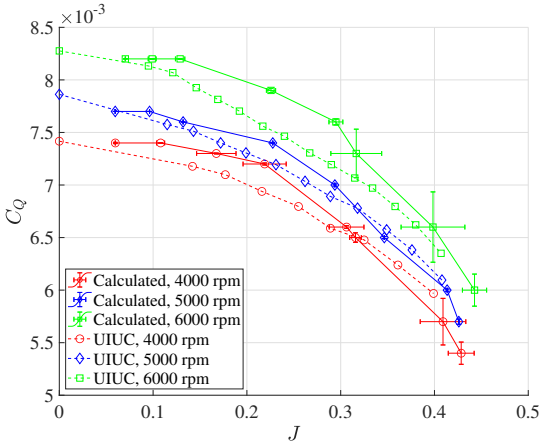

Figure 20 – Calculated torque coefficient curve of APC10x4.7SF

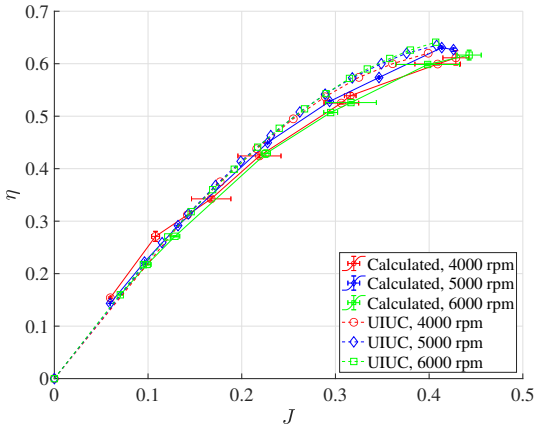

Figure 21 – Calculated propulsion efficiency curve of APC10x4.7SF

5.6 Measured Propeller Characteristics

Figure 22–30 show the propeller characteristics obtained from the whirling arm experiments. Measured characteristics were almost consistent with the wind tunnel experiments' data through the proposed correction. The standard deviation of the torque is rather large, but it does not affect the accuracy of the measured value.

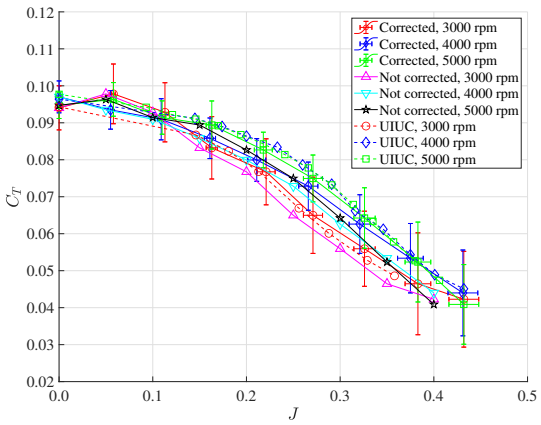

Figure 22 – Measured thrust coefficient curve of APC10x5E

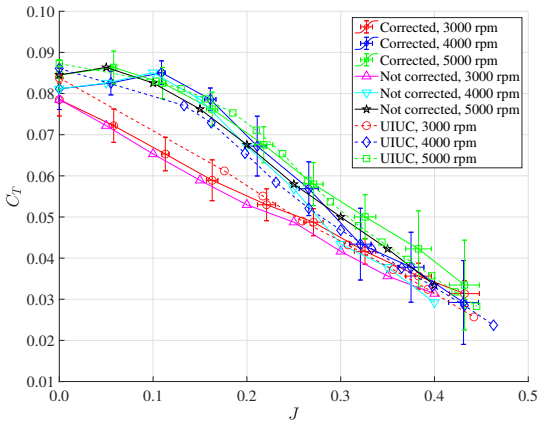

Figure 23 – Measured thrust coefficient curve of APC11x4.5E

6. Conclusion

In this work, the authors showed the modeling of the induced velocities of the wakes of the propeller on the whirling arm. The authors also produced the correction of the characteristics obtained from the whirling arm experiment using the velocity model. The effectiveness of the both results were evaluated by the numerical investigation and application to the experimental data.

The results of the numerical investigation showed good consistency with the UIUC results. Furthermore, it was demonstrated that the correction of the measured characteristics would be consistent with the wind tunnel experiments' data. These facts suggest that the whirling arm will be useful to analyze the propeller characteristics at low advance ratios.

7. Acknowledge

The authors would like to thank M. Kikuchi, technical staff of Iwate university for the development of the research equipment. This work is partly supported by KAKENHI (18K04192) and the discretionary expense of the dean of the faculty of science and engineering, Iwate university, and Soft-Path Engineering Research Center (SPERC), faculty of science and engineering, Iwate university.

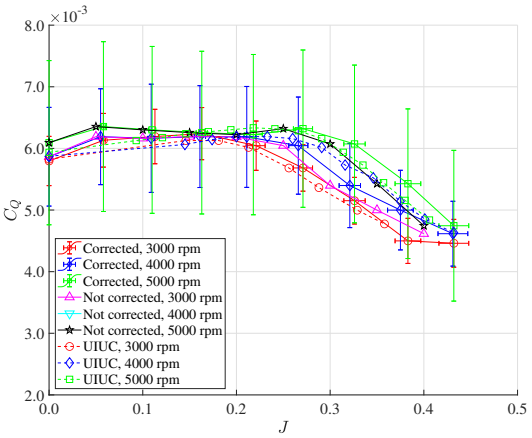

Figure 24 – Measured torque coefficient curve of APC10x5E

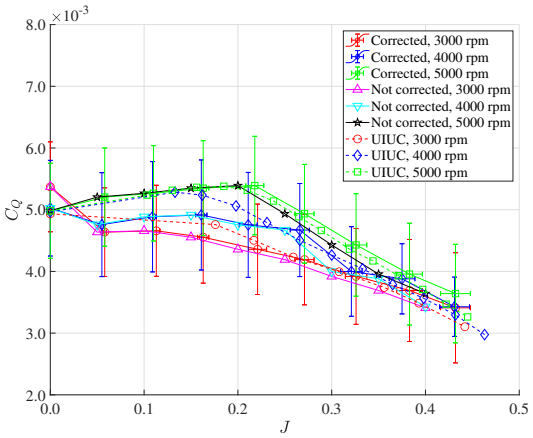

Figure 25 – Measured torque coefficient curve of APC11x4.5E

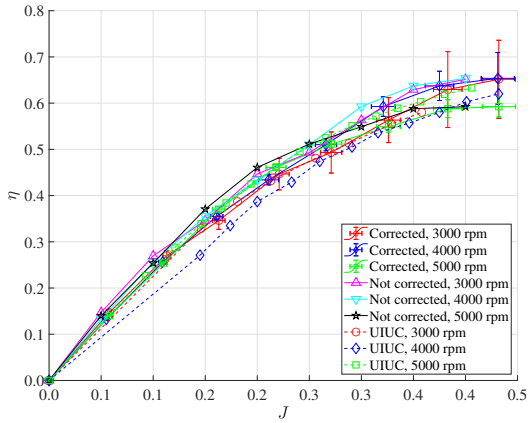

Figure 26 – Measured propulsion efficiency curve of APC10x5E

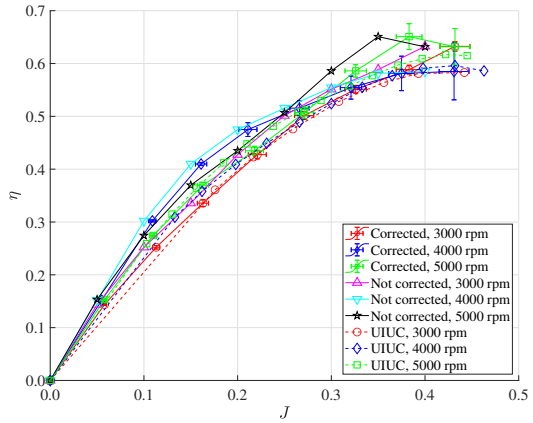

Figure 27 – Measured propulsion efficiency curve of APC11x4.5E

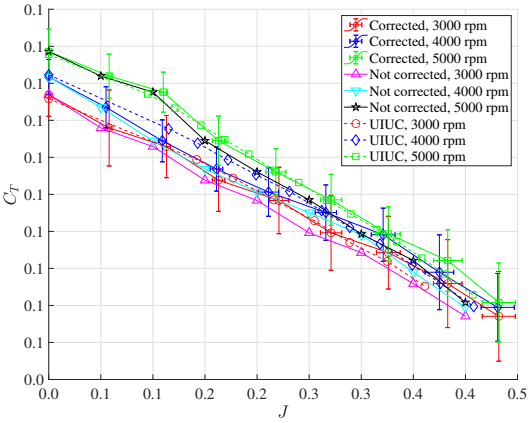

Figure 28 – Measured thrust coefficient curve of APC10x4.7SF

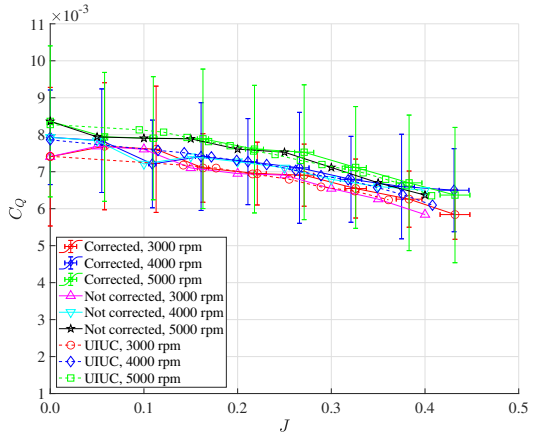

Figure 29 – Measured torque coefficient curve of APC10x4.7SF

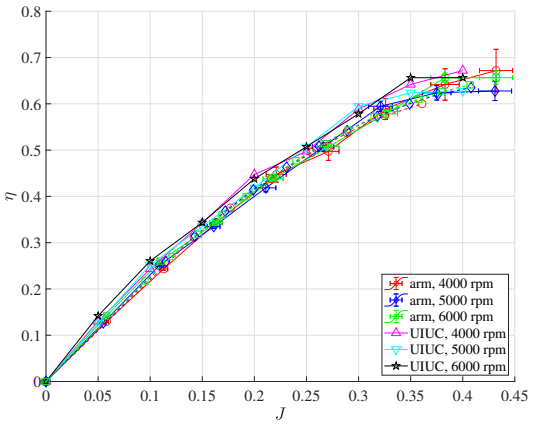

Figure 30 – Measured propulsion efficiency curve of APC10x4.7SF

8. Contact Author Email Address

mailto: t5718002@iwate-u.ac.jp

9. Copyright Statement

References

[1] Silvestre M., Morgado J, Alves P, Santos P, Gamboa P and Pascoa J. Propeller Performance Measurements at Low Reynolds Numbers. *International Journal of Mechanics*. Vol. 9, pp. 154-166, 2015.

[2] Brandt J and Selig M. Propeller performance data at low Reynolds numbers. *Proceedings of the 49th AIAA Aerospace Sciences Meeting Including the New Horizons Forum and Aerospace Exposition*, Orlando, Florida, United State of America, AIAA paper 2011-1255, 2011.

[3] McCrink M and Gregory J. Blade element momentum modeling of low-Re small UAS electric propulsion systems. *Proceedings of the 33rd AIAA Applied Aerodynamics Conference*, Dallas, Texas, United State of America, AIAA paper 2015-3296, 2015.

[4] Itoh Y. Measurement of propeller characteristics at low advance ratio using a whirling arm with brake, *Proceedings of the 55th Aircraft Symposium*, Matsue, Japan, JSASS-2017-5023, 2017 (in Japanese).

[5] Itoh Y and Satoh A. Measurement of propeller characteristics at a negative advance ratio using a whirling arm facility. *Proceedings of the 2018 Asia-Pacific International Symposium on Aerospace Technology (APISAT 2018)*, Vol. 459, pp. 1169-1188, 2019.

[6] Itoh Y. and Satoh A (in press). Modeling and numerical investigation of aerodynamic characteristics of a propeller circling on a whirling arm. *Transactions of the Japan Society for Aeronautical and Space Sciences*.

[7] Okulov V and Sorensen J. Stability of helical tip vortices in a rotor far wake. *Journal of Fluid Mechanics*, Vol. 576, pp. 1-25, 2007.

[8] Saffman P. *Vortex dynamics*. 1st edition, Cambridge University Press, 1992.

[9] Khan W and Nahon M. A propeller model for general forward flight conditions. *International Journal of Intelligent Unmanned Systems*, Vol. 3, No. 2, pp. 72-92, 2015.

[10] Adkins C and Liebeck R. Design of optimum propellers. *Journal of Propulsion and Power*. Vol. 10, No. 5, pp. 676-682, 1994.

[11] McCormick B. *Aerodynamics, aeronautics, and flight mechanics*. 1st edition, John Wiley & Sons, 1979.

[12] UIUC Propeller Data Site, https://m-selig.ae.illinois.edu/props/propDB.html (accessed May 3, 2019).